ORNL/TM-2022/1847

Testing and Simulation of an Updated Cartridge Loop Vehicle

Jacob P. Gorton
A. Shay Chapel
David K. Felde
Daniel C. Sweeney
Joel L. McDuffee

May 2022

OAK RIDGE National Laboratory

ORNL IS MANAGED BY UT-BATTELLE LLC FOR THE US DEPARTMENT OF ENERGY

ORNL/TM-2022/1847

Nuclear Energy and Fuel Cycle Division

TESTING AND SIMULATION OF A CARTRIDGE LOOP IRRADIATION VEHICLE

Jacob P. Gorton
A. Shay Chapel
David K. Felde
Daniel C. Sweeney
Joel L. McDuffee

May 2022

Prepared by
OAK RIDGE NATIONAL LABORATORY
Oak Ridge, TN 37831-6283
managed by
UT-BATTELLE LLC
for the
US DEPARTMENT OF ENERGY
under contract DE-AC05-00OR22725

CONTENTS

FIGURES

TABLES

ABSTRACT

The Versatile Test Reactor (VTR) is a sodium-cooled, fast-spectrum test reactor being developed in the United States that will support a variety of irradiation test vehicle configurations, including cartridge loops. This work includes out-of-pile experimental results from a single-phase, natural circulation cartridge loop vehicle with geometry relevant to VTR irradiation sites, as well as comparisons between the experimental results and results predicted via the TRAC/RELAP Advanced Computational Engine (TRACE) modeling tool. The experiments were conducted in the thermosyphon test loop (TSTL) facility at Oak Ridge National Laboratory. Comparisons were also made between the current experimental data and results from natural circulation experiments previously conducted in the TSTL in a cartridge vehicle that is similar in design but has smaller flow areas. This cartridge vehicle and the experimental program were developed to add to the single-phase, natural circulation data collected in the previous iteration of the cartridge loop design, which supports future irradiation experiments and adds to a database useful for validating computer models. Comparing experimental results to TRACE model predictions is a pertinent step in validating the computational tool for supporting future irradiation experiment design and safety calculations, and comparisons to previous cartridge loop results highlight the effect of the design changes on the test vehicle. The experiments conducted included several steady-state tests and transients, including power ramp, loss of off-site power, and loss of external flow scenarios. This work showed that TRACE can accurately predict temperatures and flow conditions in the cartridge loop and that the updated vehicle design achieves higher mass flow rates at the same steady-state power levels.

LIST OF ACRONYMS AND NOMENCLATURE

ACRONYMS

BN – boron nitride
FRS – fuel rod simulator
ID – inner diameter
LOOP – loss of offsite power
NRC – Nuclear Regulatory Commission
OD – outer diameter
rRMSE – relative root-mean-square error
TC – thermocouple
TRACE – TRAC/RELAP Advanced Computational Engine
TSTL – Thermosyphon Test Loop
VTR – Versatile Test Reactor

NOMENCLATURE

A = area
ρ = density
ΔP = differential pressure
k = form loss coefficient
u = velocity
D_h = hydraulic diameter
μ = dynamic viscosity
ν = kinematic viscosity
g = gravitational constant
β = coefficient of linear thermal expansion
T = temperature
ΔT = differential temperature
$\dot{m}$ = mass flow rate
Re = Reynolds number
Gr = Grashof number
f_D = Darcy friction factor
P = power
N = number of data points
x = Experimental datapoint
y = simulated datapoint

Subscripts

o = relating to the orifice plate
$fluid$ = relating to a fluid property
FRS = relating to the FRSs
max = maximum
min = minimum
0 = initial or reference value
s = FRS surface
i = iterator

1. INTRODUCTION

The Versatile Test Reactor (VTR) is being designed to enable fast neutron irradiation experiments that support nuclear reactor technology development. The 300 MW_{th} sodium-cooled fast reactor will support several types of irradiation test devices, including instrumented and uninstrumented substitutional test assemblies and cartridge vehicles (Wachs et al., 2018; McDuffee et al., 2019). This work details out-of-pile experimental data from a newly designed natural circulation cartridge loop vehicle that is geometrically consistent with VTR's irradiation sites. Collecting experimental data for cartridge loop vehicles is essential for validating computer models for future experiment design and safety calculations in VTR. This work also compared the experimental data with predictions from the US Nuclear Regulatory Commission's (NRC's) TRAC/RELAP Advanced Computational Engine (TRACE), which further supports code validation for future experiment design and qualification. The final objective of this work is to compare the experimental data from the updated cartridge with results from a previous iteration of the cartridge vehicle that was similar in design but had smaller coolant flow areas (Petrie et al., 2020). Both cartridges used a thermosyphon cooling system, used single-phase water as the working fluid, and were tested in the Thermosyphon Test Loop (TSTL) facility at Oak Ridge National Laboratory.

Cartridge loop test vehicles are being included in the scope of potential VTR experiment types because they create an irradiation environment that is isolated from the primary reactor coolant. This isolation allows for any advanced reactor coolant—including sodium, molten salts, helium, and lead—to be irradiated in VTR without contaminating the primary sodium coolant and offers more control over the thermal hydraulic environment than test assemblies in direct contact with the reactor coolant (McDuffee et al., 2017; Petrie et al., 2020). However, the achievable temperatures in a cartridge loop are limited by the amount of heat that can be rejected to the primary reactor coolant.

The thermosyphon cartridges used in the TSTL experiments in this work and in Petrie et al. (2020) have no internal pumping components and rely on natural circulation to remove heat from the water in the inner thermosyphon loop to the flowing cooling flow in the outermost annulus. VTR cartridge vehicles are expected to require an internal pump to remove enough heat from the loop working fluid during normal operation while simultaneously achieving relevant flow conditions for some reactor coolants, such as molten salts (Hunning et al., 2019; Gorton et al., 2022). However, the natural circulation data collected in this work are still relevant for validating computer models and examining potential accidents, such as loss of off-site power (LOOP) or loss of forced cooling events.

2. METHODOLOGY

2.1 TSTL AND CARTIDGE LOOP DESCRIPTION

The TSTL comprises the primary cartridge vessel and an external flow loop, which acts as the heat sink for the experiment. Figure 1 shows a schematic of the TSTL facility, and Figure 2 shows a detailed view of the thermosyphon cartridge vehicle and the internal components. Within the cartridge is a central baffle pipe and two annular flow channels; the inner annulus acts as a downcomer in the natural circulation loop, and the outer annulus allows coolant from the TSTL to enter the cartridge and remove heat. The baffle pipe and the downcomer are connected at the top by an open cooling vessel and at the bottom by an orifice plate with small openings, and this loop is isolated from the outermost annulus. Three electrically heated fuel rod simulators (FRSs) are inserted at the lower region of the baffle pipe and cause the working fluid within the inner flow channel to flow upward through natural convection. The fluid spills over the top of the baffle pipe into the cooling vessel and then flows downward around the baffle pipe through the downcomer region. Fluid then reenters the baffle pipe through the openings in the cylindrical orifice plate. This type of buoyancy-aided flow loop is referred to as a *thermosyphon*. A helium cover gas

pumped into the top of the cooling vessel pressurized the internal natural convection loop to approximately 100 psig at room temperature for all tests conducted in the updated thermosyphon. The updated thermosyphon is rated to a maximum pressure of 250 psig, and 225 psig was used as the pressure limit during the experiments. Heat transfer between the water and the cover gas causes the system pressure to rise during the experiments. Starting with 100 psig at room temperature roughly maximized the peak achievable power in the cartridge without exceeding 225 psig and without boiling the water during the experiments. In the previous experiments conducted in Petrie et al. (2020), the initial fill gas pressure ranged from roughly 30 to 860 psig, depending on the test type.

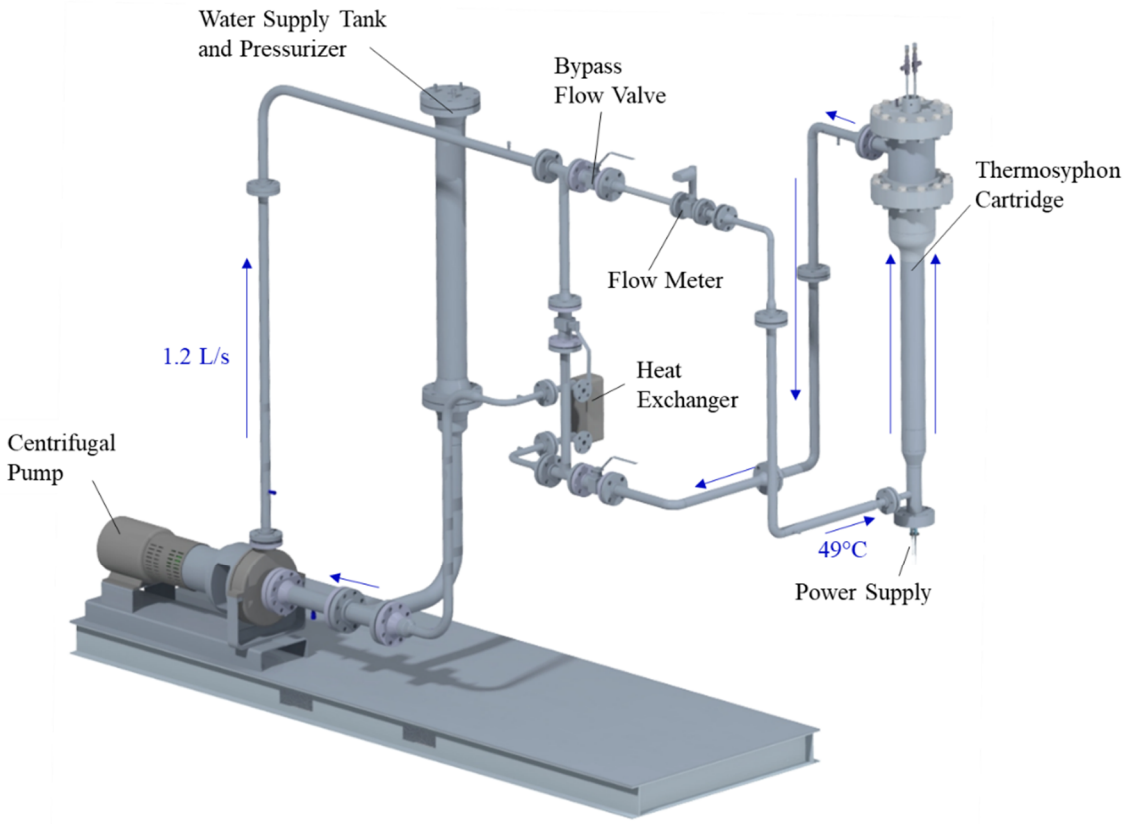

Figure 1. Schematic of the TSTL.

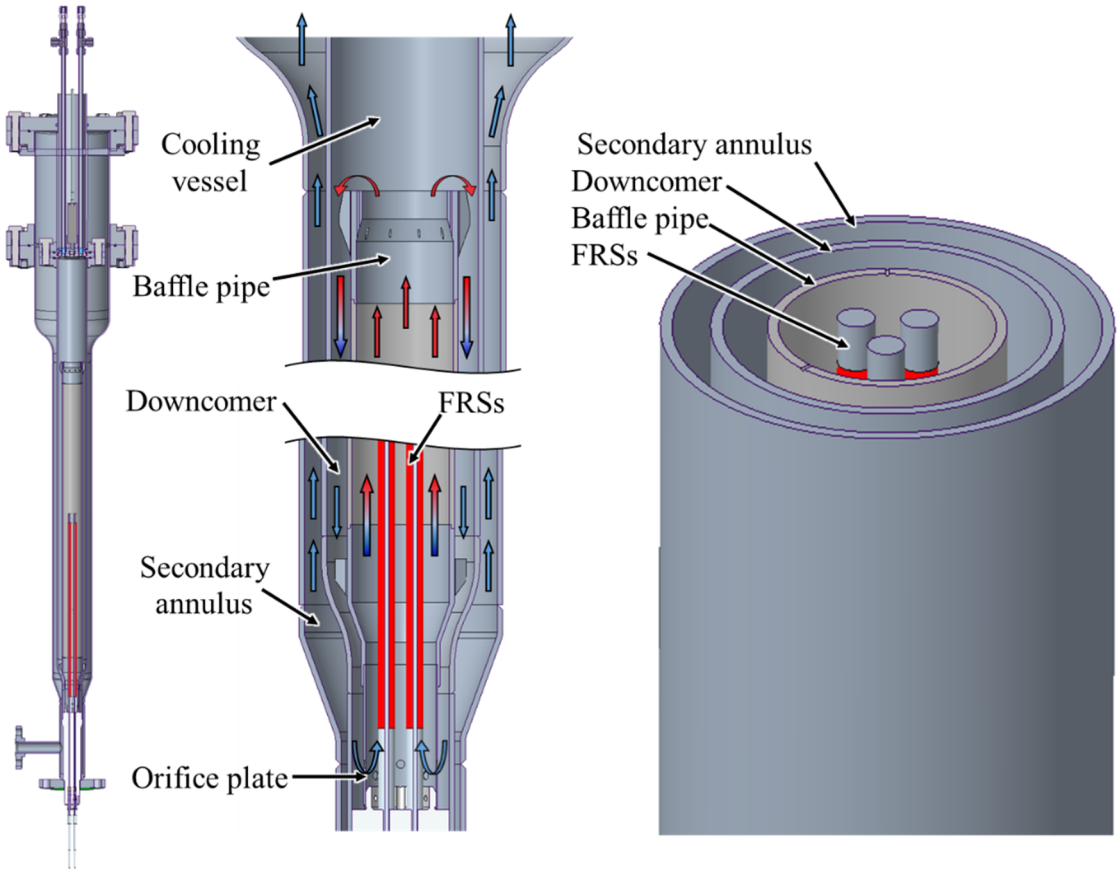

Figure 2. Detailed diagram of the thermosyphon cartridge vehicle.

Coolant from the external loop enters the outermost annular flow channel at the bottom of the thermosyphon at about 50°C at a nominal flow rate of 1.2 L/s. The TSTL was originally designed to qualify cartridge loops for irradiation testing in the High Flux Isotope Reactor at Oak Ridge National Laboratory, and the coolant pressure, temperature, and flow rate in the secondary system are representative of an irradiation site in that reactor (McDuffee et al., 2019). The secondary system coolant flows upward around the closed natural convection loop. This mimics the flow direction of VTR and is a notable difference from previous TSTL experiments in which the coolant entered at the top of the vessel and flowed downward. The purpose for this design change was to replicate conditions expected in VTR as closely as possible. The secondary system comprises a water pressurizer, a heat exchanger, a variable frequency drive centrifugal pump, and instrumentation to measure the secondary system coolant flow rate, temperatures, and pressures at the inlet and outlet of the thermosyphon. There is also a bypass valve that allows for flow rate control during transient experiments.

The FRSs are 9.5 mm in diameter and have a nickel alloy core surrounded by boron nitride (BN) insulation and an Inconel 718 heating filament designed to provide a uniform axial power shape. Another layer of BN separates the heating filament from an outer sheath made of Inconel 600. A DC power supply controlled by a programmable logic controller supplied power to the FRSs during experimentation. The total length of the rods was 0.579 m, and the heated length was 0.508 m. Six thermocouples (TCs) were placed along the length of each of the FRSs in a helical arrangement separated by an azimuthal angle of 60° (18 total TCs). The FRS TCs were embedded on the inner surface of the Inconel sheath. Ten TCs were placed around the natural convection loop to measure the liquid temperature. All TCs were Type N with a 1 mm outer diameter (OD) sheath. Table 1 lists the axial location of the TCs relative to the bottom

of the FRS heated length and is a useful reference for future modeling activities. Figure 3 shows the locations of the TCs in the system. A single FRS is shown in the figure for clarity.

Table 1. Locations of FRS and fluid TCs relative to the bottom of the FRS heated length (x = 0 m). FRS TC locations identical to those reported in McDuffee et al. (2017) and Petrie et al. (2020).

TC designation	Axial location (m)	Description
TE-11	0.508	TC1 on FRS 1
TE-12	0.419	TC2 on FRS 1
TE-13	0.328	TC3 on FRS 1
TE-14	0.239	TC4 on FRS 1
TE-15	0.149	TC5 on FRS 1
TE-16	0.061	TC6 on FRS 1
TE-21	0.478	TC1 on FRS 2
TE-22	0.389	TC2 on FRS 2
TE-23	0.300	TC3 on FRS 2
TE-24	0.208	TC4 on FRS 2
TE-25	0.119	TC5 on FRS 2
TE-26	0.031	TC6 on FRS 2
TE-31	0.447	TC1 on FRS 3
TE-32	0.358	TC2 on FRS 3
TE-33	0.269	TC3 on FRS 3
TE-34	0.180	TC4 on FRS 3
TE-35	0.089	TC5 on FRS 3
TE-36	0.0	TC6 on FRS 3
TE-41	0.254	Temperature at heated length midplane in baffle pipe radial center
TE-42	0.254	Temperature at heated length midplane near baffle pipe wall
TE-43	0.521	Temperature above heated length in baffle pipe radial center
TE-44	0.521	Temperature above heated length near baffle pipe wall
TE-45	-0.010	Baffle pipe inlet temperature
TE-46	0.254	Temperature at heated length midplane in downcomer
TE-47	0.521	Temperature above heated length in downcomer
TE-48	0.950	Temperature near baffle pipe outlet
TE-49	1.001	Temperature near cooling vessel inner wall
TE-50	1.001	Temperature near cooling vessel radial center

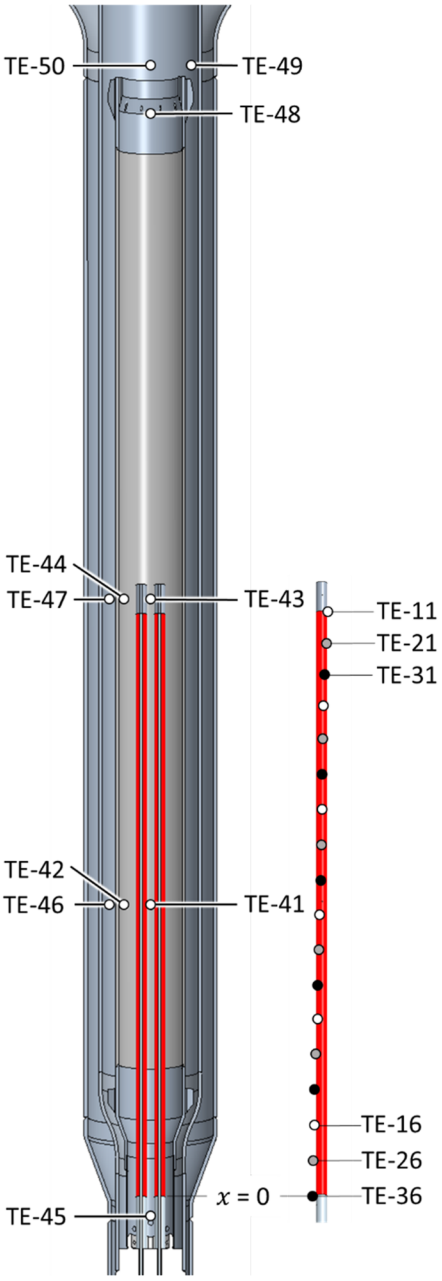

Figure 3. Depiction of TC locations. A single FRS is shown for clarity.

Two pressure sensors were located at the bottom of the thermosyphon, one on each side of the orifice plate, and additional differential pressure sensors were located approximately 3.3 cm apart on each side of the orifice place to measure the pressure drop across the orifice. The differential pressure sensor was used to determine the mass flow rate of water in the loop due to natural circulation using Eq. (1):

$$\dot{m} = A_o \sqrt{\frac{2\rho \Delta P}{k_o}}, \tag{1}$$

where A_o is the total cross-sectional flow area through the orifice plate, ρ is the water density based on the TC reading nearest the orifice plate, ΔP is the differential pressure sensor reading, and k_o is the form

loss coefficient through the orifice plate. The Reynolds, *Re*, and Grashof, *Gr*, numbers can be calculated using Eqs. (2)–(4):

$$Re = \frac{\rho u D_h}{\mu}, \tag{2}$$

$$Gr = \frac{g\beta(T_s - T_0)D_h^3}{\nu^2}, \tag{3}$$

$$\beta = \frac{1}{\rho_0}\left(\frac{\rho_0 - \rho_s}{T_s - T_0}\right), \tag{4}$$

where u is the fluid velocity, D_h is the hydraulic diameter, g is acceleration due to gravity, μ is the dynamic viscosity, ν is the kinematic viscosity of water, β is the linear coefficient of thermal expansion, T_s is the FRS outer surface temperature, and T_0 is the fluid temperature far away from the heat source.

In McDuffee et al. (2017), an orifice flow test facility was used to determine the pressure drop across the orifice plate based on the volumetric flow rate. In Petrie et al. (2020), a fit was calculated to the data that resulted in a form loss coefficient of 1.765 ± 0.014 for the orifice plate. The same orifice plate is used in the updated thermosyphon, and the form loss coefficient was assumed to be the same. The updated thermosyphon cartridge uses the same FRSs and instruments as the previous designs with the addition of more fluid temperature TCs. Uncertainty values for the instruments used in the TSTL are given in McDuffee et al. (2017) and in the supplemental data files provided in Petrie et al. (2020) for previous thermosyphon iterations. Uncertainty in the temperature and differential pressure sensor measurements, the loss coefficient, and the orifice plate cross-sectional area based on engineering drawing tolerances were propagated into mass flow rate, Reynolds number, and Grashof number calculations.

The primary changes made in the updated thermosyphon compared with the design used in Petrie et al. (2020) are that the TSTL coolant flows upward through the outer annulus, the baffle pipe and downcomer are longer, the cooling vessel is shorter, and the baffle pipe, downcomer, and outer annulus diameters are larger. The updated thermosyphon was also designed to support and inline pump to allow for forced convection tests, although the pump was not installed for this work. Table 2 lists the key dimensional changes between the updated thermosyphon and the previous design.

Table 2. Dimensional comparison between updated and previous thermosyphon designs.

Dimension	Updated design value (cm)	Previous design value (cm)
Baffle pipe inner diameter (ID)	5.48	3.96
Baffle pipe OD	6.03	4.14
Downcomer ID	8.28	4.93
Downcomer OD	8.89	6.05
Outer annulus ID (around cooling vessel)	21.2	10.8
Outer annulus OD (around cooling vessel)	21.9	17.5
Outer annulus ID (around downcomer)	10.8	6.71
Outer annulus OD (around downcomer)	11.4	7.32
Baffle pipe and downcomer length	102.1	67.1
Cooling vessel length	30.7	80.8
Outer annulus inlet to outlet length	162.8	162.8

2.2 TRACE MODEL DESCRIPTION

TRACE v5.0 Patch 5 was used to model the thermosyphon cartridge and a portion of the external flow loop for the code-to-experiment comparisons. TRACE is an NRC tool that could be used for qualifying future VTR experiments, so using it in this work to begin validating the code against experimental data for this application is relevant. The primary hydraulic components considered in the model were the baffle pipe, cooling vessel, downcomer, orifice plate, and secondary annulus containing flow from the external loop. Some additional piping was modeled before and after the secondary annulus component. Instead of modeling the entire external flow loop, a TRACE fill component was used to control the coolant conditions entering the secondary annulus, and a break component was used as an infinite outlet sink for the secondary annulus. The coolant conditions entering the secondary annulus were programmed to match the experimental conditions so that any measured changes in inlet temperature or flow rate could be captured in the models.

The baffle pipe, downcomer, and secondary annulus were modeled as 1D pipes, and the cooling vessel was modeled using a TRACE vessel component. For this analysis, only one radial and one azimuthal region were considered in the vessel, making it effectively 1D. However, the use of a vessel for this structure instead of another pipe allowed for two pipes—the baffle and the downcomer—to be connected to the same face of the vessel. The thermosyphon loop was filled with water to halfway up the cooling vessel length in the experiments and the TRACE model. The upper half of the vessel was filled with helium gas at 100 psig at room temperature before conducting the experiments. The orifice plate between the downcomer and the baffle pipe was modeled as a zero-length junction and was assigned the nominal form loss coefficient of 1.765 calculated in previous work (McDuffee et al., 2017; Petrie et al., 2020). Figure 4 provides a schematic of the TRACE model developed in the Symbolic Nuclear Analysis Package (Jones et al., 2009) alongside a physical representation of the thermosyphon for reference.

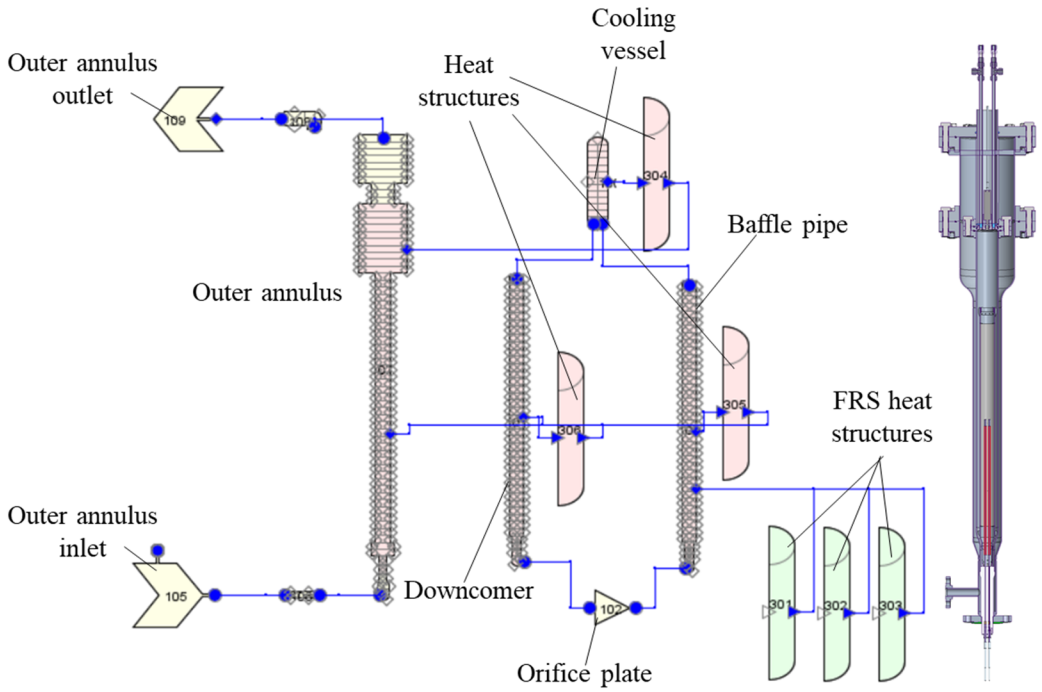

Figure 4. TRACE model schematic.

Additional form losses in the natural convection loop resulted from abrupt cross-sectional flow area changes and friction factors. TRACE automatically calculates form loss coefficients due to abrupt expansions and contractions in cross-sectional flow area using Eqs. (5) and (6), respectively (U.S. NRC, 2017):

$$k_{exp} = \left(1 - \frac{A_{min}}{A_{max}}\right)^2 \tag{5}$$

$$k_{con} = 0.5 - 0.7\left(\frac{A_{min}}{A_{max}}\right) + 0.2\left(\frac{A_{min}}{A_{max}}\right)^2, \tag{6}$$

where k signifies the form loss coefficient, A_{min} is the minimum cross-sectional flow area at an abrupt area change, and A_{max} is the maximum cross-sectional flow area at an abrupt area change. Equations (7) and (8) are the expressions for TRACE's default Darcy friction factors for laminar and turbulent flow, which were used for this analysis:

$$f_D = \frac{64}{Re}, \tag{7}$$

$$f_D = \frac{0.316}{Re^{0.25}}, \tag{8}$$

where f_D is the Darcy friction factor, and Re is the Reynolds number. In these experiments, Re was ranged from 0 to a maximum of approximately 15,000.

2.3 EXPERIMENTAL PROGRAM

The TSTL experiments can be classified into one of five types, which are summarized in Table 3. The first type of experiment included multiple step increases in FRS power up to a maximum value of 27.4 kW. Temperatures in the thermosyphon were allowed to reach steady state at each power interval. Steady state was assumed to have been reached when the variation in TC readings was less than their associated uncertainty values of ±0.5°C. The maximum power caused the cartridge pressure to nearly reach the 225 psig limit without boiling. The other test types were transients and included gradual loss of external flow tests, rapid loss of external flow tests, LOOP scenarios, and power ramps. Figure 5 shows the power and external loop mass flow rate, $\dot{m}$, during one trial of each test type. All three gradual loss of external flow tests were run consecutively and are all shown in Figure 5(B). Except for the rapid loss of external flow test, these test types were also conducted in Petrie et al. (2020). The present report compares the natural circulation flow rates, Reynolds numbers, and fluid temperatures for the steady-state intervals, gradual loss of external flow, and LOOP tests. Direct comparisons could not be made for the power ramp tests because of significant differences in ramp rates and because boiling was observed in the power ramp tests conducted in Petrie et al. (2020). The previous experiments did not consider loss of external flow experiments with constant power.

Table 3. Summary of experimental program.

Test type	General description	Number of trials	Power range	External loop flow rate
A	Steady-state power intervals	1	0–27.4 kW in step-intervals	1.18 kg/s
B	Gradual loss of external flow	3	15, 10 and 5 kW	1.18 kg/s (initial) decreased to ~0.13–0.19 kg/s
C	Rapid loss of external flow	2	15 and 20 kW	1.18 kg/s (initial) decreased to 0.32 kg/s
D	LOOP scenario	6	Initial power of 10 and 15 kW (3 trials each)	1.18 kg/s (initial) decreased to 0.32 kg/s
E	Power ramp	2	Ramp from 0 to 15 and 20 kW	1.18 kg/s

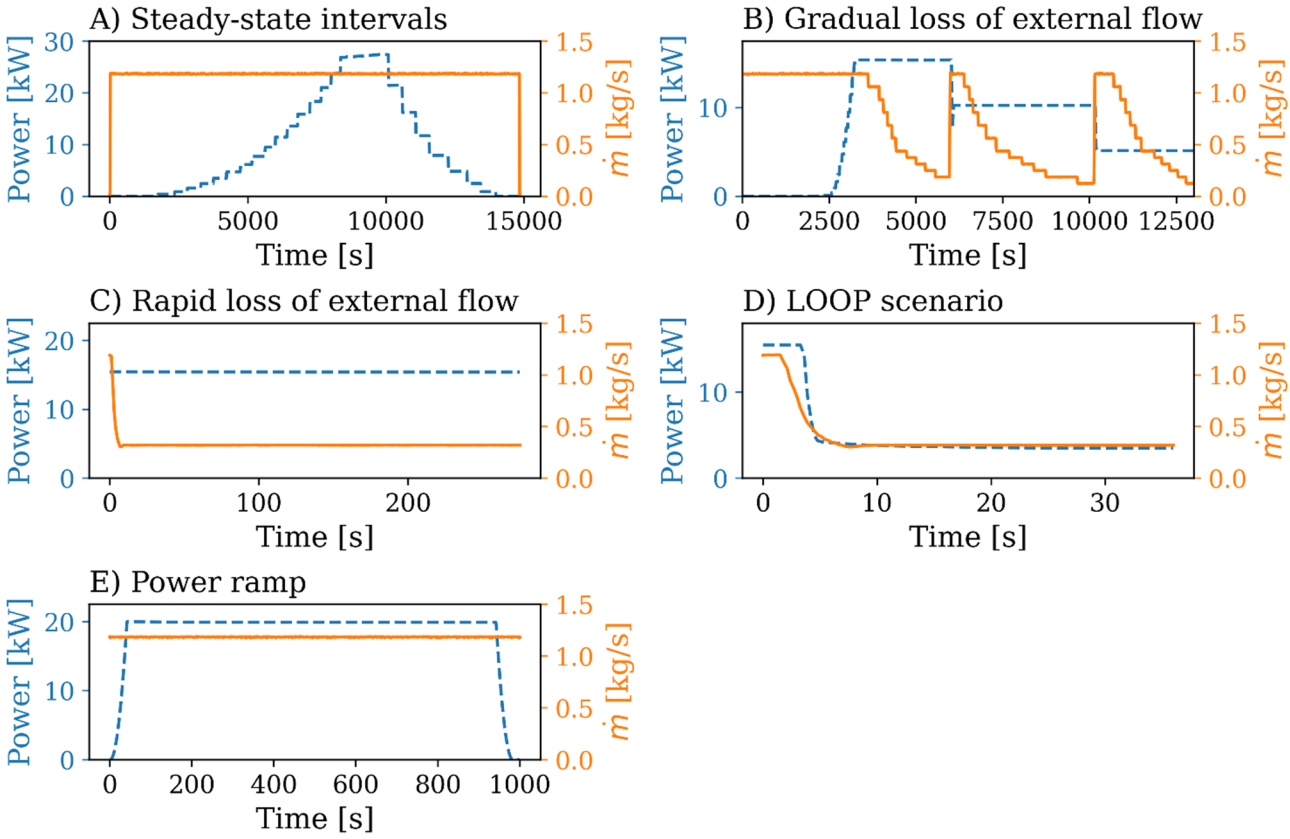

Figure 5. Power and external loop mass flow rate from one trial of each test type.

3. RESULTS

3.1 CARTRIDGE CHARACTERIZATION AND COMPARISON WITH PREVIOUS THERMOSYPHON DESIGN

Figure 6 shows the TC readings during the heating portion of the steady-state interval test. The data were filtered so that only steady-state temperature values are shown. The saturation temperature, T_{sat}, is also plotted, which shows that the peak water temperature approached but did not exceed the T_{sat} at the maximum power. The thermal gradient between the baffle pipe inlet temperature (TE-45) and the peak water temperature (TE-44) grew with power, which is indicative of the increasing natural circulation mass flow rate and enhanced heat removal. At the maximum power level, the difference between the TE-45 and TE-44 measurements was 88.5°C, and the subcooling between T_{sat} and TE-44 was 9.6°C.

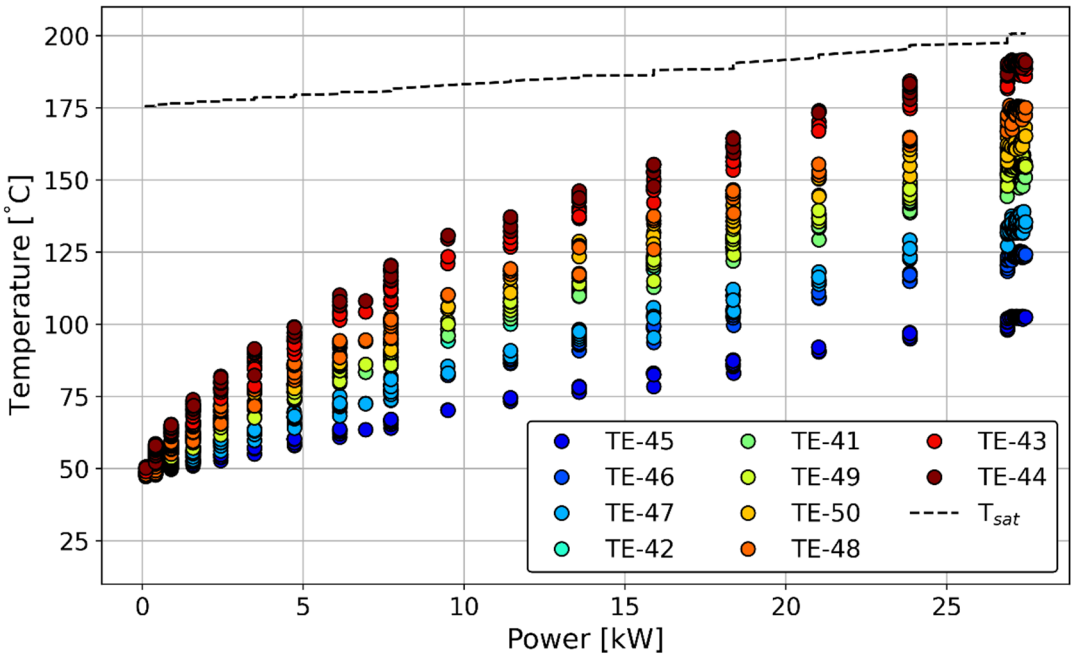

Figure 6. Steady-state water temperatures as a function of total FRS power.

Figure 7 shows a comparison of the inlet and maximum fluid temperatures in the updated and previous thermosyphon designs during steady-state tests. The peak water temperature was roughly the same in both cartridge designs for power less than 15 kW, and the previous design exhibited higher temperatures above 15 kW. The water entering the baffle was at a noticeably lower temperature in the updated thermosyphon design because of enhanced cooling capabilities, which led to a larger temperature difference between the minimum and maximum water temperatures in the baffle. The minimum-to-maximum temperature difference is plotted in Figure 8.

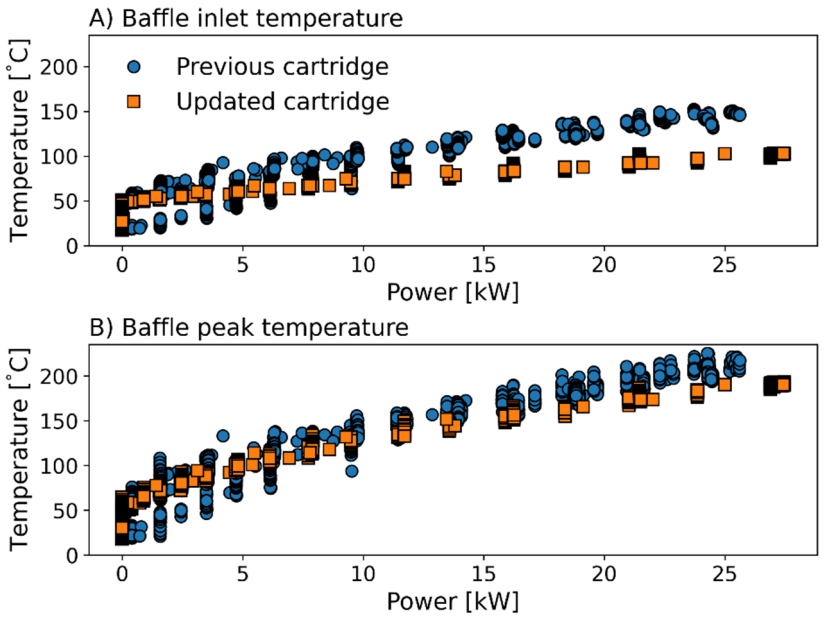

Figure 7. Comparison of inlet and peak fluid temperatures in the baffle pipe.

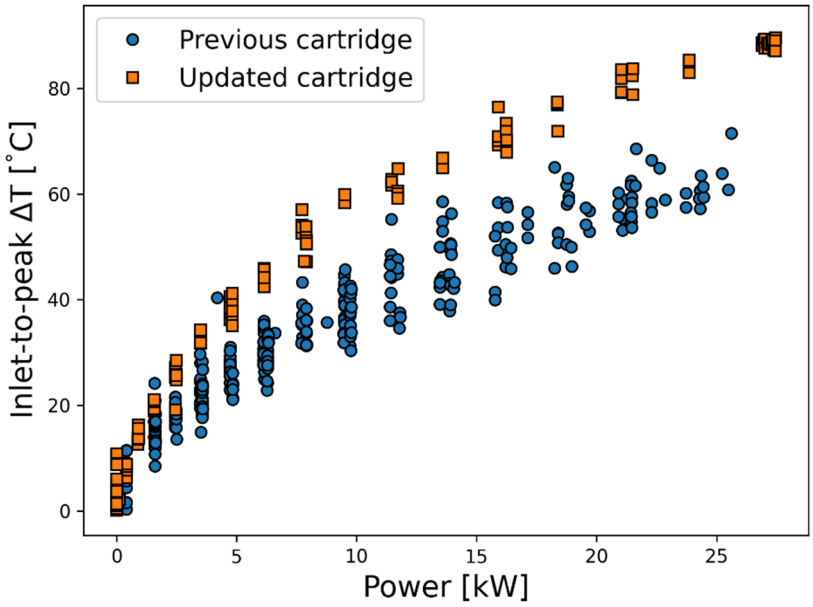

Figure 8. Comparison of minimum-to-maximum differences in baffle pipe water temperature.

Greater fluid temperature differences between the hot and cold legs in a thermosyphon promote natural circulation. This effect is shown in Figure 9, which shows that the nominal mass flow rates in the updated cartridge design are somewhat greater than those in the previous design. The error bars in the figure account for propagated uncertainty from each of the terms in Eq. 1, which was used to calculate the mass flow rate based on the orifice plate geometry, calibrated form loss coefficient, water density, and differential pressure sensor measurement. Despite having greater mass flow rates, Figure 10 shows that the Reynolds numbers in each design are approximately the same across all power levels. The error bars in this figure account for the propagated uncertainty in each term in Eq. 2. This approximately equal

Reynolds numbers are due to the higher fluid temperatures in the previous thermosyphon and the sensitivity of the dynamic viscosity of water. The relatively rapid decrease in dynamic viscosity with increasing temperatures roughly canceled out the greater mass flow rate and cross-sectional flow area in the updated cartridge design.

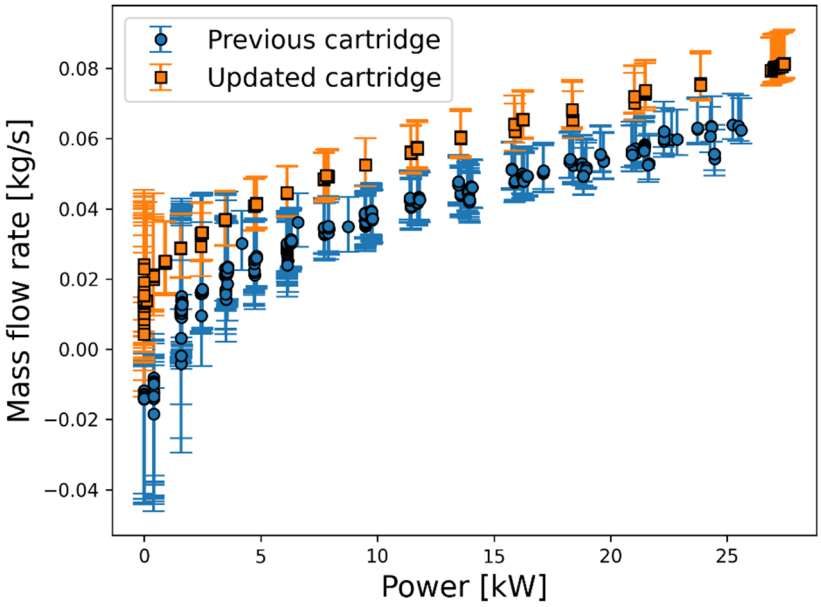

Figure 9. Comparison of mass flow rates in the cartridge.

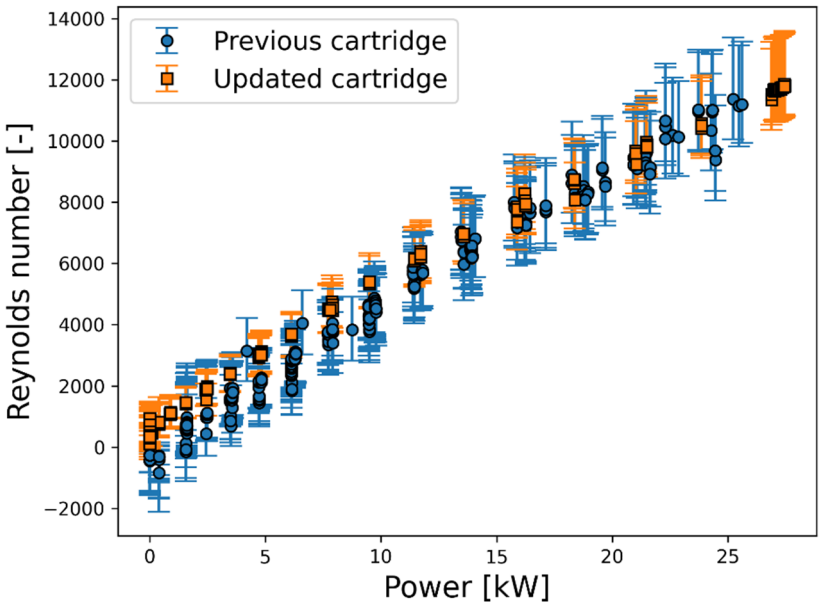

Figure 10. Comparison of Reynolds numbers.

The Grashof number comparison is shown in Figure 11, again accounting for propagated uncertainty in the terms in Eq. 3. In this case, the updated cartridge has significantly higher values, which are caused by

the larger pipe diameter and the D_h^3 term in Eq. (3). The values for β and $T_s - T_0$ were greater in the previous cartridge design, but the difference in D_h^3 had the dominant effect. However, Grashof numbers shown in Figure 11 were calculated based on the hydraulic diameters in the rodded region of the baffle pipe, which were 1.91 cm for the previous cartridge design and 3.83 cm for the updated design. Figure 12 shows the Grashof number comparison using hydraulic diameters from the empty baffle pipe region. In this region, the difference in D_h^3 is not as profound, and the Grashof numbers are more similar. In the empty baffle region, the hydraulic diameters are equivalent to the baffle pipe IDs and are 3.96 cm for the previous design and 5.48 cm for the updated design.

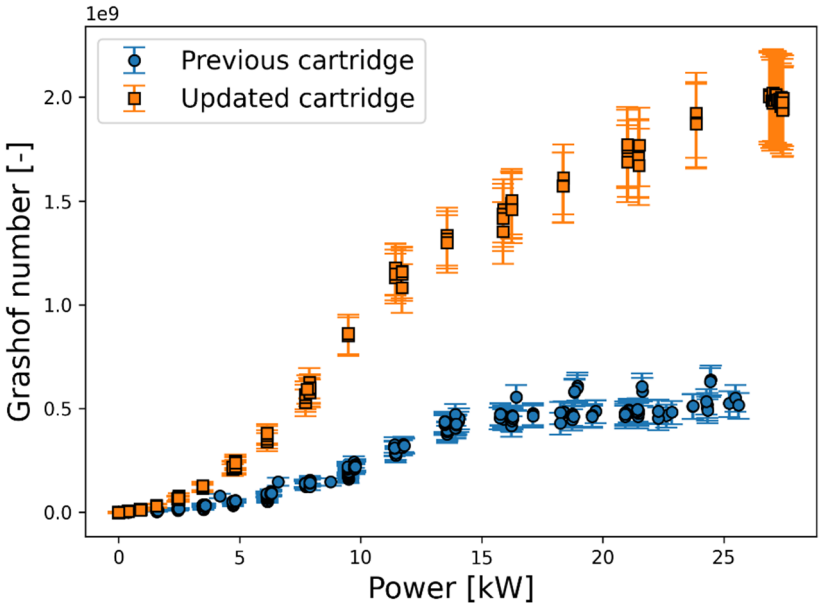

Figure 11. Comparison of Grashof numbers.

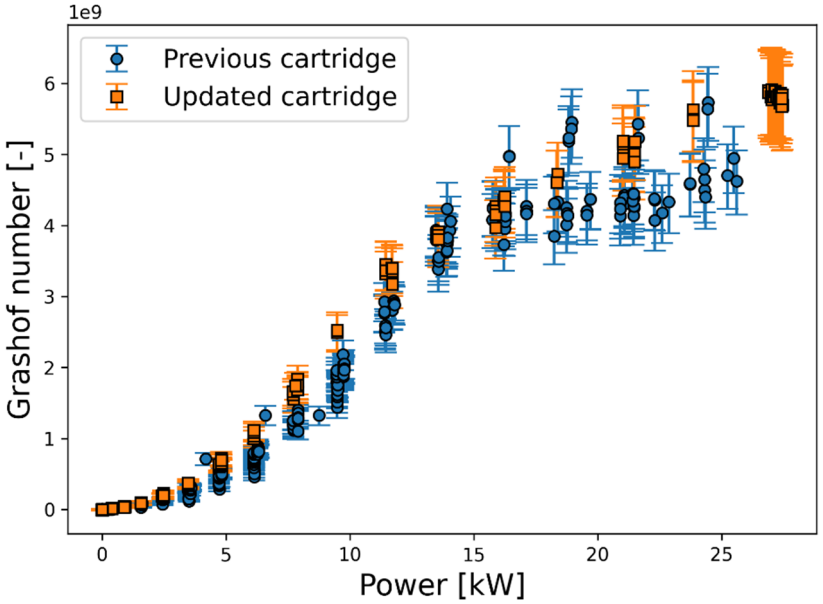

Figure 12. Grashof number comparison in the empty baffle pipe region.

The trends in the steady-state comparisons generally also applied to the transient tests. This is shown in Figure 13 through Figure 17 for the LOOP tests with an initial power (P_0) = 15 kW. Figure 13 shows that both the baffle inlet and maximum water temperatures are lower in the updated thermosyphon, and Figure 14 shows that the minimum-to-maximum ΔT is initially greater in the updated thermosyphon but declines faster during the transient. Figure 15 shows that the natural circulation mass flow rate in the updated cartridge design is greater during the steady-state initialization of the LOOP event, and the nominal mass flow rate predictions are greater throughout the transient than the previous design. However, there is considerable overlap in the uncertainty bars between the two designs. The Reynolds number predictions in Figure 16 are similar between the two cartridge designs. There is a 5–20 s period during which the previous thermosyphon has greater mass flow rates, but this is due to the power being removed from the system at a slower rate. Grashof numbers are compared in Figure 17 by using the hydraulic diameters in the rodded region of the baffle pipe. Referencing the steady-state Grashof numbers in Figure 12, the initial Grashof number in both designs would increase to roughly 4×10^9 if the diameters from the empty baffle region were used.

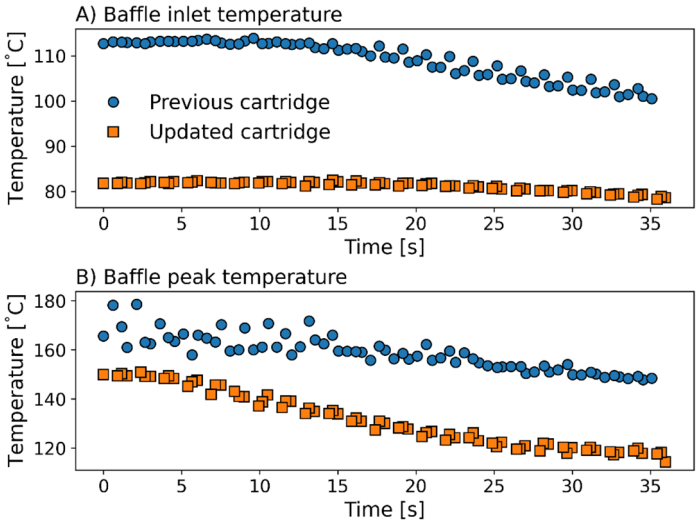

Figure 13. Baffle inlet and peak fluid temperatures during LOOP tests with P_0 = 15 kW.

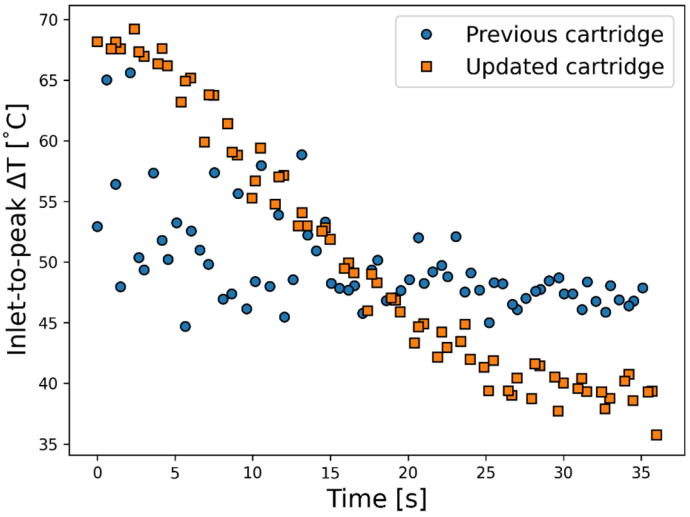

Figure 14. Minimum-to-maximum water temperature differences during LOOP tests with P_0 = 15 kW.

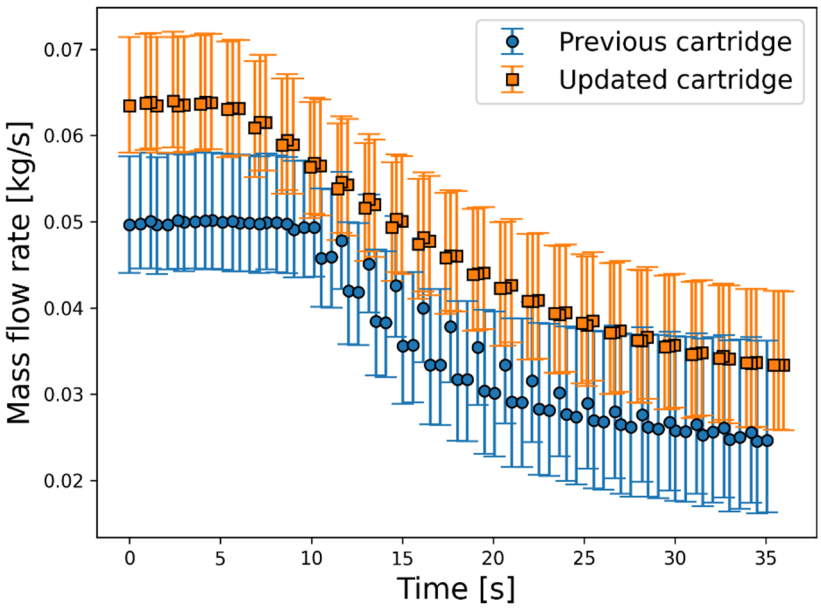

Figure 15. Comparison of mass flow rates during LOOP tests with P_0 = 15 kW.

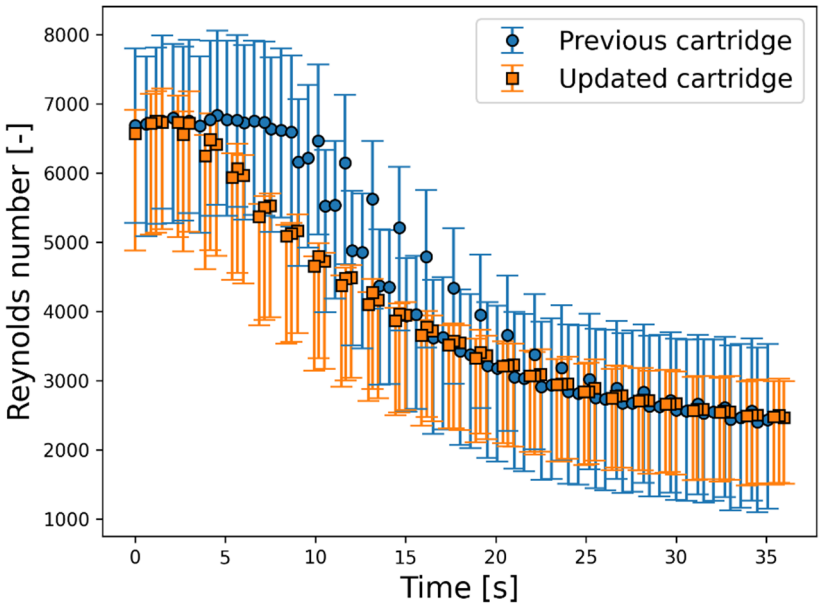

Figure 16. Comparison of Reynolds numbers during LOOP tests with P_0 = 15 kW.

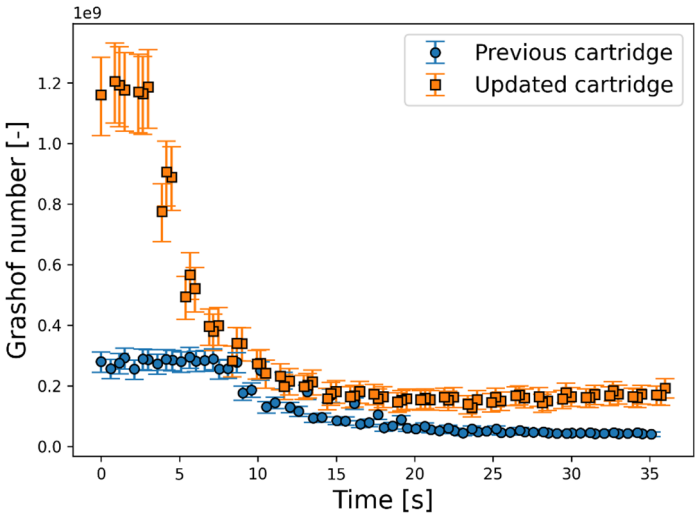

Figure 17. Comparison of Grashof numbers during LOOP tests with P_0 = 15 kW.

Comparisons between the previous and updated cartridge designs were not made for the power ramp tests or the external loss of flow with constant power. The power ramp tests conducted in Petrie et al. (2020) used a much slower power ramp rate, had a peak power of 80 kW (compared with 20 kW in the updated design), and boiling was shown to have occurred. Each of these factors precluded a like-for-like comparison. Loss of external flow tests with constant power were not conducted in the previous design. Results from these tests in the updated thermosyphon are presented here.

Two power ramp tests were conducted. The first went to a maximum power (P_{max}) of 15 kW, and the other went to P_{max} = 20 kW. Power was increased at a rate of 0.5 kW/s in both tests. Figure 18 shows the ΔT between the baffle pipe inlet and maximum water temperatures during the power ramp tests. Figure 19 through Figure 21 show the natural circulation mass flow rates, Reynolds numbers, and Grashof numbers, respectively, during the power ramp tests. These figures show that there is a slight overshoot of the steady-state mass flow rate value during the test, but this did not result in higher Reynolds or Grashof numbers than the steady-state values.

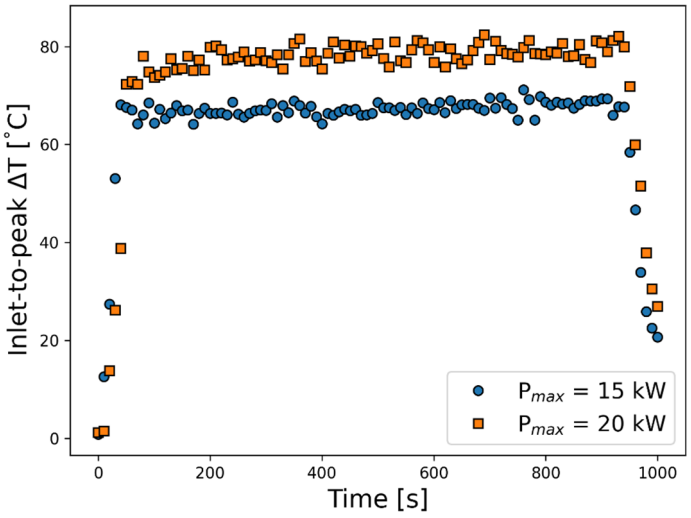

Figure 18. Inlet-to-maximum fluid temperature differences during power ramp tests.

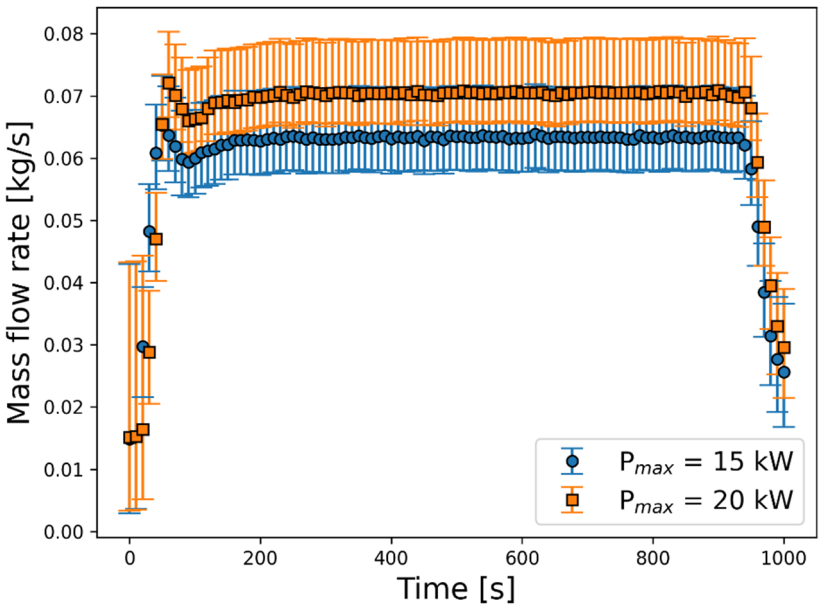

Figure 19. Mass flow rates during power ramp tests.

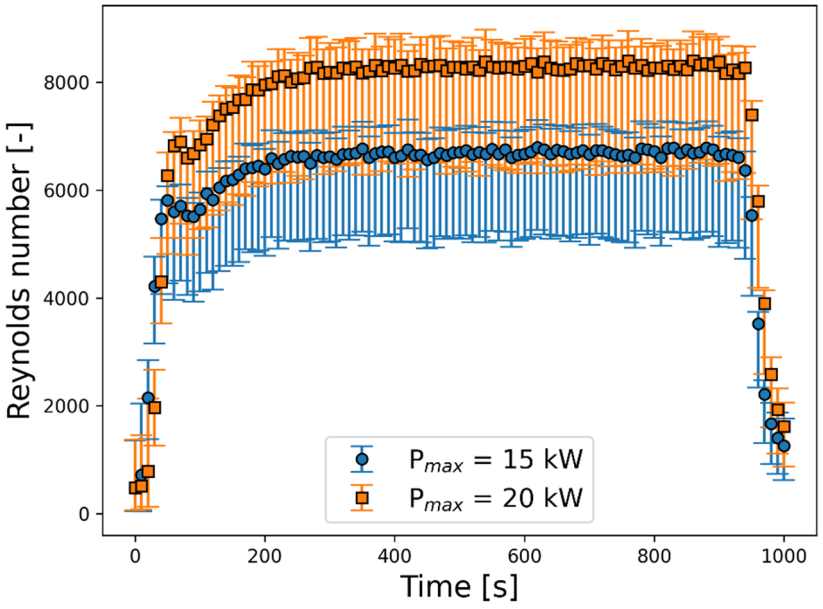

Figure 20. Reynolds numbers during power ramp tests.

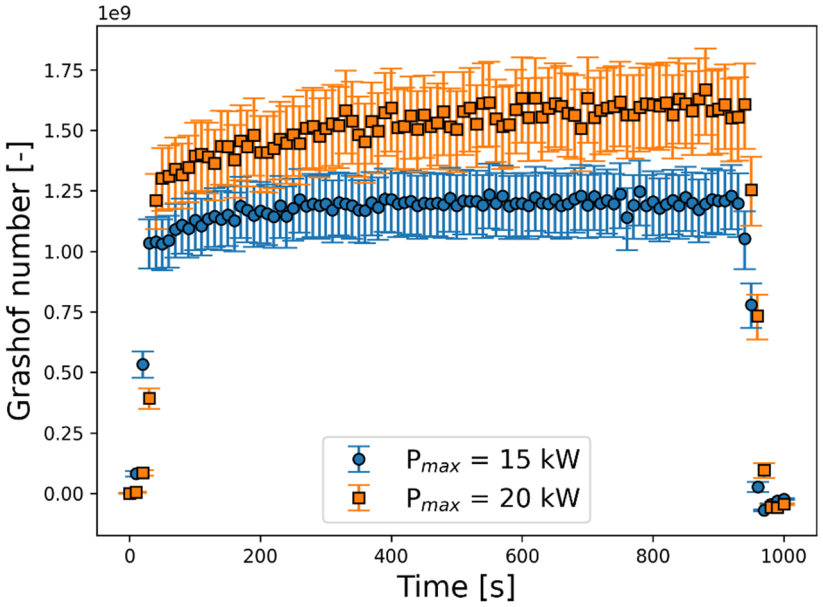

Figure 21. Grashof numbers during power ramp tests.

Two loss of external flow tests at constant power were conducted, and the power levels for the two tests were 15 and 20 kW. The external loop flow rate was reduced from the nominal 1.2 L/s to 0.32 L/s over 8 s. Figure 22 shows the baffle inlet and peak temperatures during the loss of external flow tests. The 15-kW test reached a new steady state at approximately 275 s, at which point the test was stopped. The 20-kW test took 190 s to reach steady state. In the 15-kW test, the inlet temperature rose by 17°C, and in the 20-kW test, the rise was 20°C. The peak temperatures rose by roughly the same amount, so there was no change in the inlet-to-maximum ΔT. Figure 23 through Figure 25 show the mass flow rates, Reynolds numbers, and Grashof numbers during the two tests. There was an initial decrease in the mass flow rate and Reynolds number in both tests, although the decline in mass flow rate was almost nearly recovered by approximately 75 s into the test. The Reynolds numbers in both tests showed a slight increase over their initial values. These changes are due to the 17–20°C temperature increase, which changed the properties of water. The Grashof numbers remained largely unchanged during the tests.

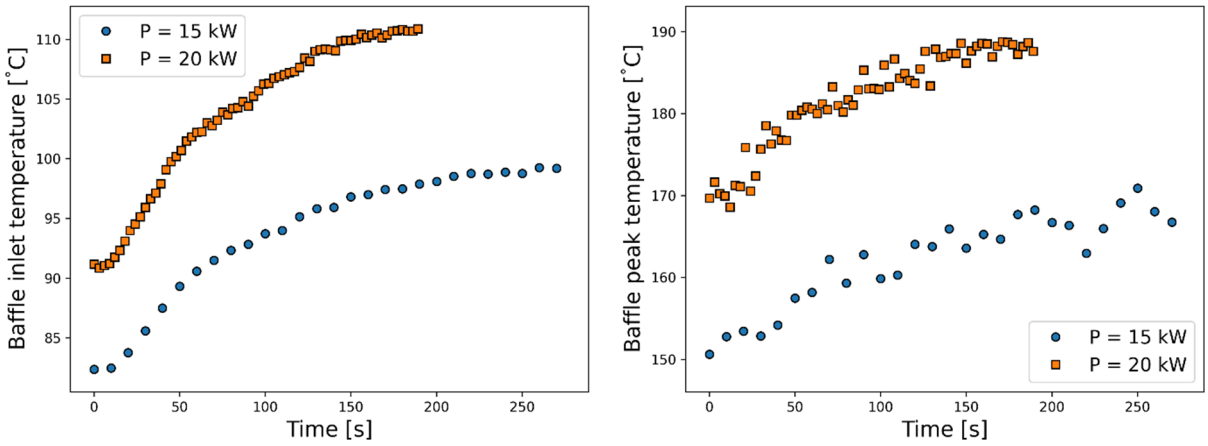

Figure 22. Baffle inlet and peak temperatures during loss of external flow tests.

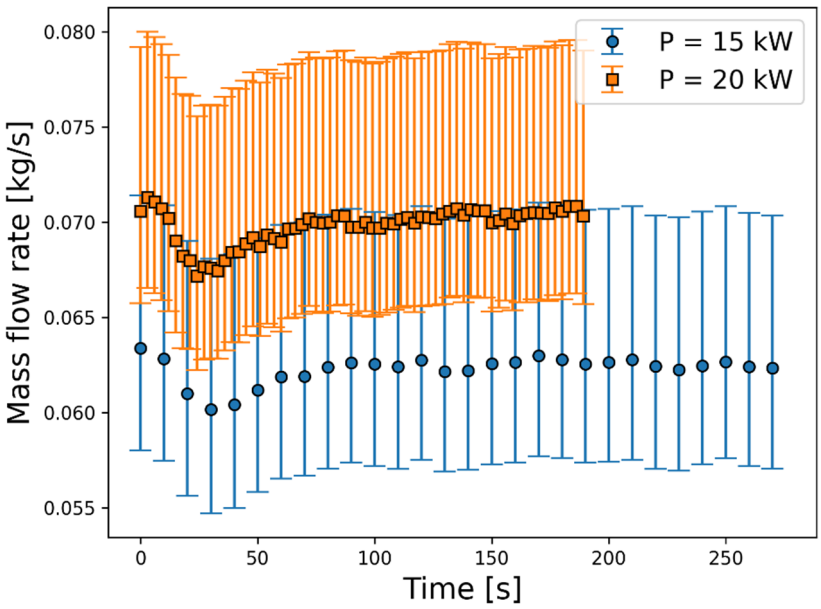

Figure 23. Mass flow rates during loss of external flow tests.

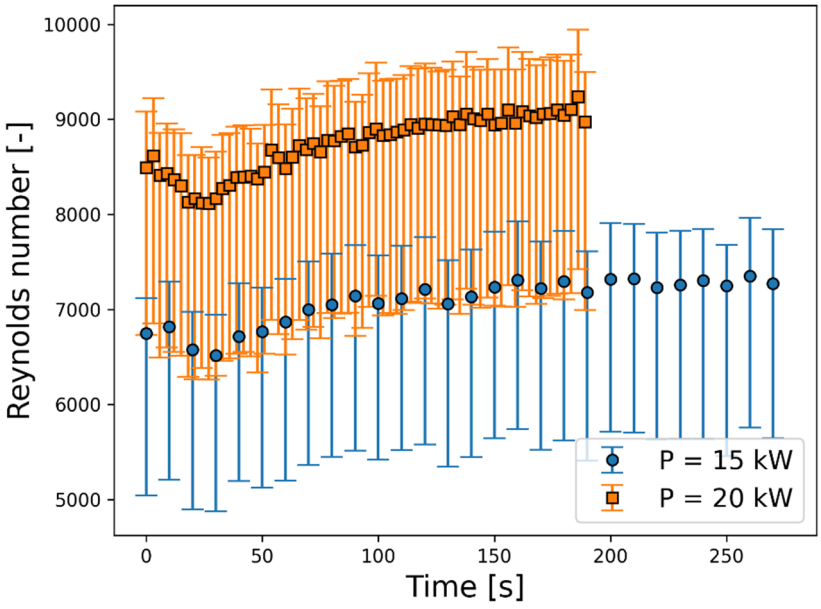

Figure 24. Reynolds numbers during loss of external flow tests.

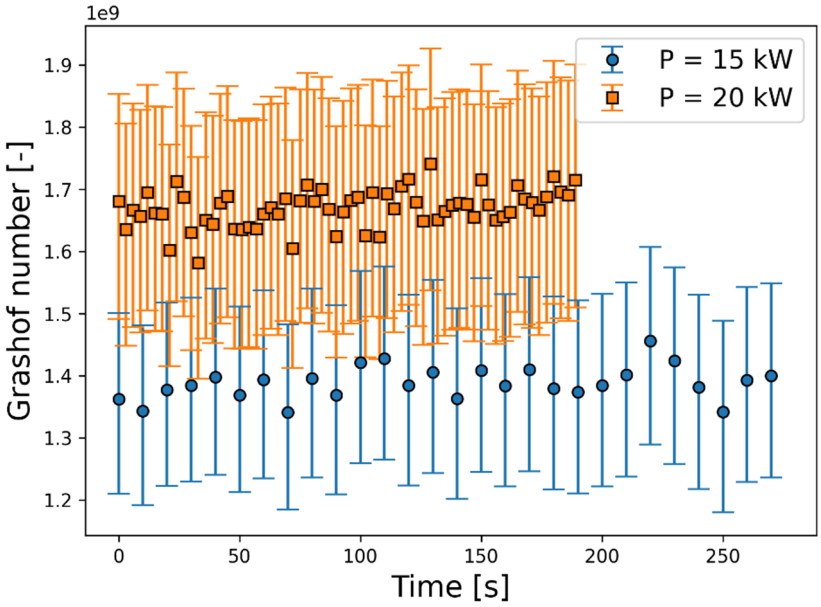

Figure 25. Grashof numbers during loss of external flow tests.

Figure 26 shows the cartridge gauge pressure during the ramp power tests and rapid loss of external flow tests. The former test type at a power of 20 kW was the limiting out of the entire experimental program in terms of approaching the 225 psig pressure limit. At the peak pressures in the 20 kW power ramp and loss of external flow tests, the saturation temperatures were 189.6 and 199.6°C, respectively. The peak water temperatures during these tests were 174.4 and 190.9°C, respectively, indicating that boiling did not occur.

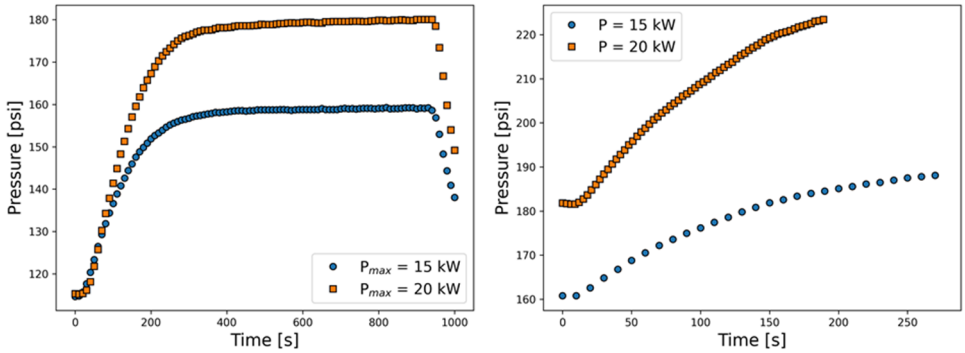

Figure 26. Cartridge pressures during (A) ramp power tests and (B) rapid loss of external flow tests.

3.2 TRACE-TO-EXPERIMENT COMPARISONS

Each test conducted using the updated thermosyphon cartridge was simulated by using the TRACE thermal hydraulics code, and comparisons between the experimental and simulated results are shown here. Figure 27 shows the comparison of peak water temperature in the baffle pipe in one of each of the five test types. Results for the rapid loss of external flow and the LOOP tests shown are from tests with initial power levels of 20 and 15 kW, respectively, and the results for the power ramp tests are from the case with P_{max} = 20 kW. Figure 27 shows high correlation between the models and the experimental data. The most consistent discrepancy occurs during the LOOP experiment in which TRACE predicts a 5–10°C

higher temperature throughout the transient. The six LOOP tests were run in series, and it is possible that this error is the result of the system not fully reaching steady state before this run was initiated.

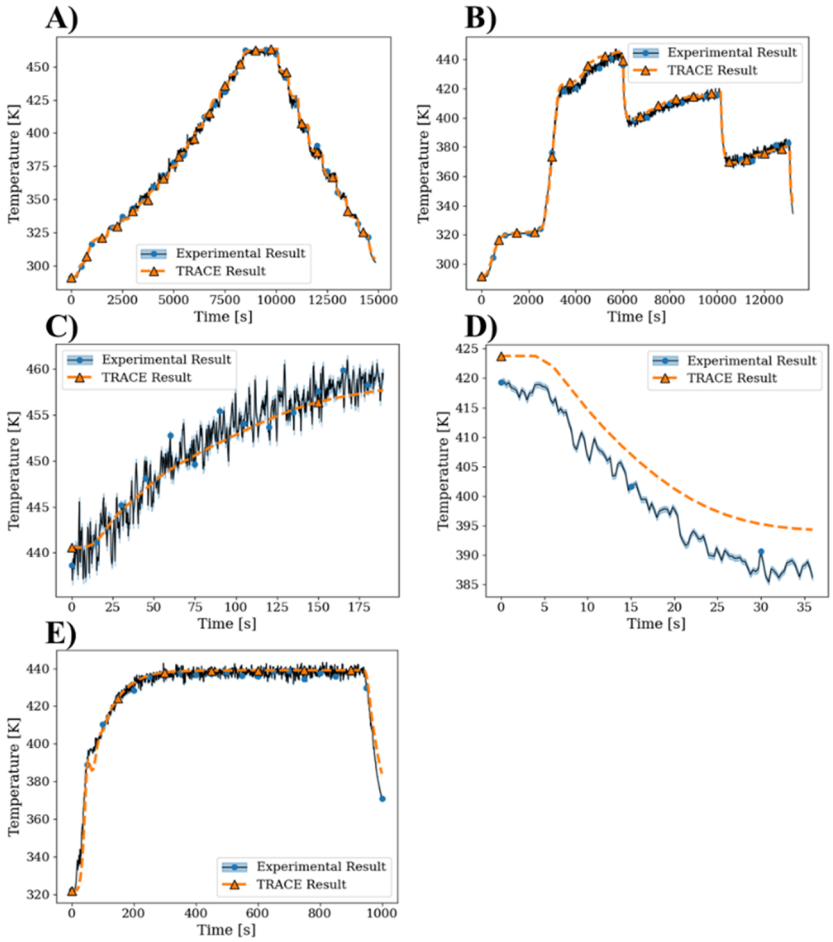

Figure 27. Comparison of peak water temperatures during the (A) steady-state interval test, (B) gradual loss of external flow test, (C) rapid loss of external flow test, (D) LOOP test, and (E) power ramp test.

Figure 28 through Figure 30 show comparisons of the mass flow rates, Reynolds numbers, and Grashof numbers, respectively, in one of each of the five test types. The TRACE predictions are typically within the uncertainty bands for the mass flow rate and Reynolds number for each test, except for the rapid loss of external flow and at the maximum power in the steady-state interval test. The uncertainty bands were derived by propagating the uncertainty in each measurement and water property and are indicated in the figures by the shaded regions. The Grashof number comparisons are also in generally good agreement, although there are more occurrences of the TRACE prediction being outside the experimental uncertainty range. Discrepancies for this parameter are due to TRACE consistently predicting higher FRS surface temperatures and the compounding effects on film temperature and the water properties associated with the film temperature.

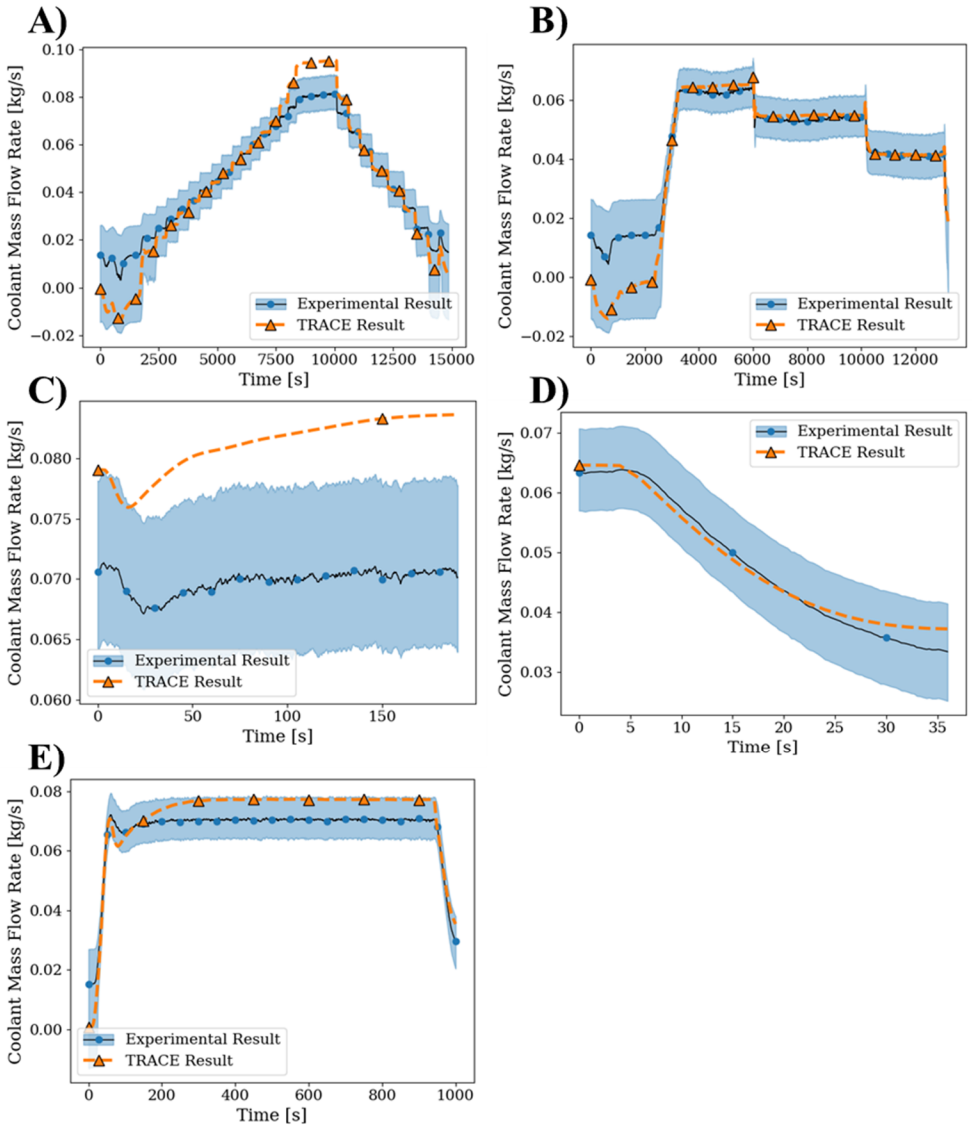

Figure 28. Comparison of mass flow rates during the 9A) steady-state interval test, (B) gradual loss of external flow test, (C) rapid loss of external flow test, (D) LOOP test, and (E) power ramp test.

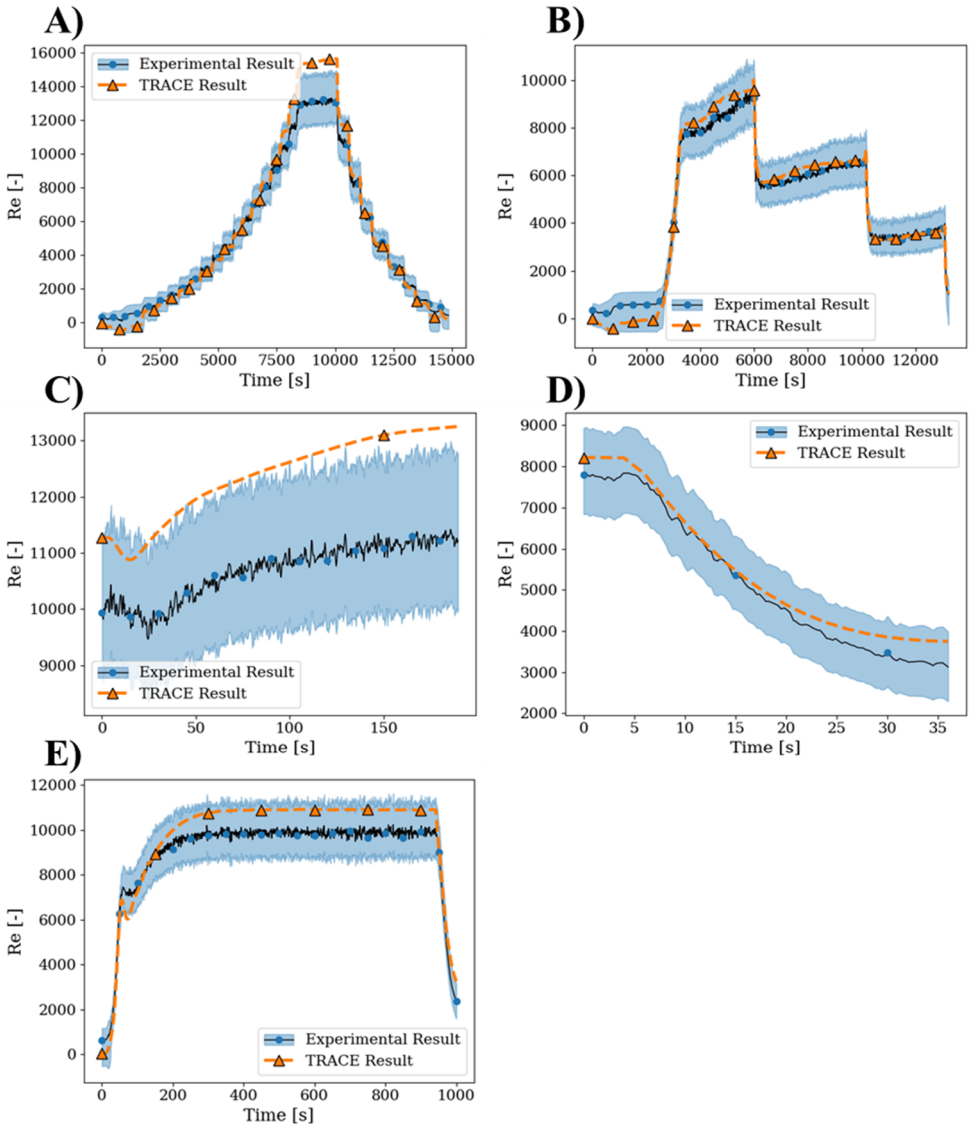

Figure 29. Comparison of Reynolds numbers during the (A) steady-state interval test, (B) gradual loss of external flow test, (C) rapid loss of external flow test, (D) LOOP test, and (E) power ramp test.

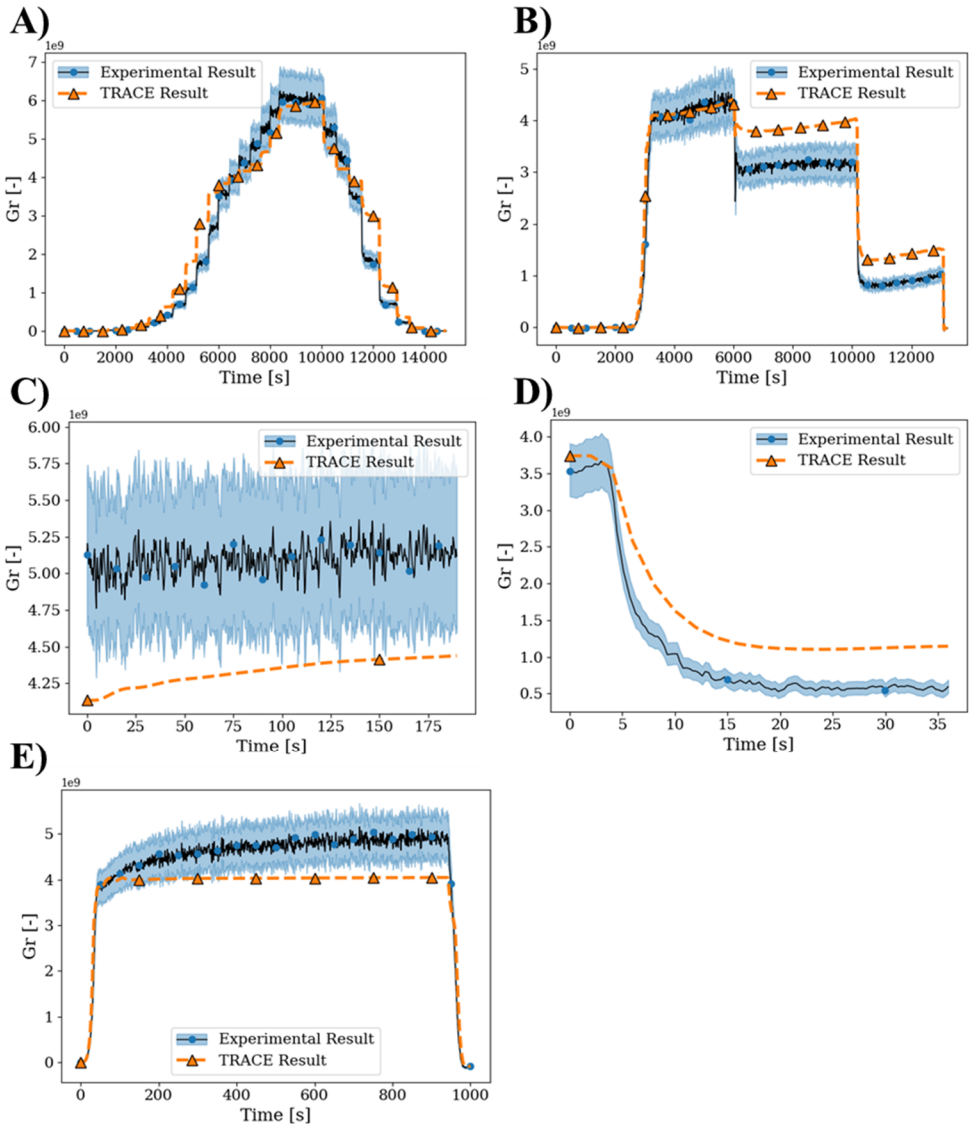

Figure 30. Comparison of Grashof numbers during the (A) steady-state interval test, (B) gradual loss of external flow test, (C) rapid loss of external flow test, (D) LOOP test, and (E) power ramp test.

Figure 31 shows code-to-experiment comparisons for the mass flow rates, water temperatures, FRS temperatures, Grashof numbers, and Reynolds numbers using data from all tests in the experimental program. The data points shown in the figure were taken every 30 s during the tests, except for in the LOOP tests in which comparison points were taken at 7, 21, and 35 s. The fluid temperature comparison includes all TCs in the cartridge loop, and the FRS temperature comparison includes all 18 FRC TCs. The relative root-mean-square error (rRMSE) was used to quantify the differences between the TRACE predictions and experimental results and is given by Eq. (9):

$$rRMSE = 100\% \times \frac{\sqrt{\frac{1}{N}\sum(x_i - y_i)^2}}{\bar{x}}, \tag{9}$$

where x_i denotes an experimental value, y_i denotes a simulated value, $\bar{x}$ denotes the mean of the experimental data, and N is the number of data points in the set. The calculation uses the nominal experimental values and does not consider uncertainty in the measurements. Table 4 shows the resulting rRMSE values for each parameter considered.

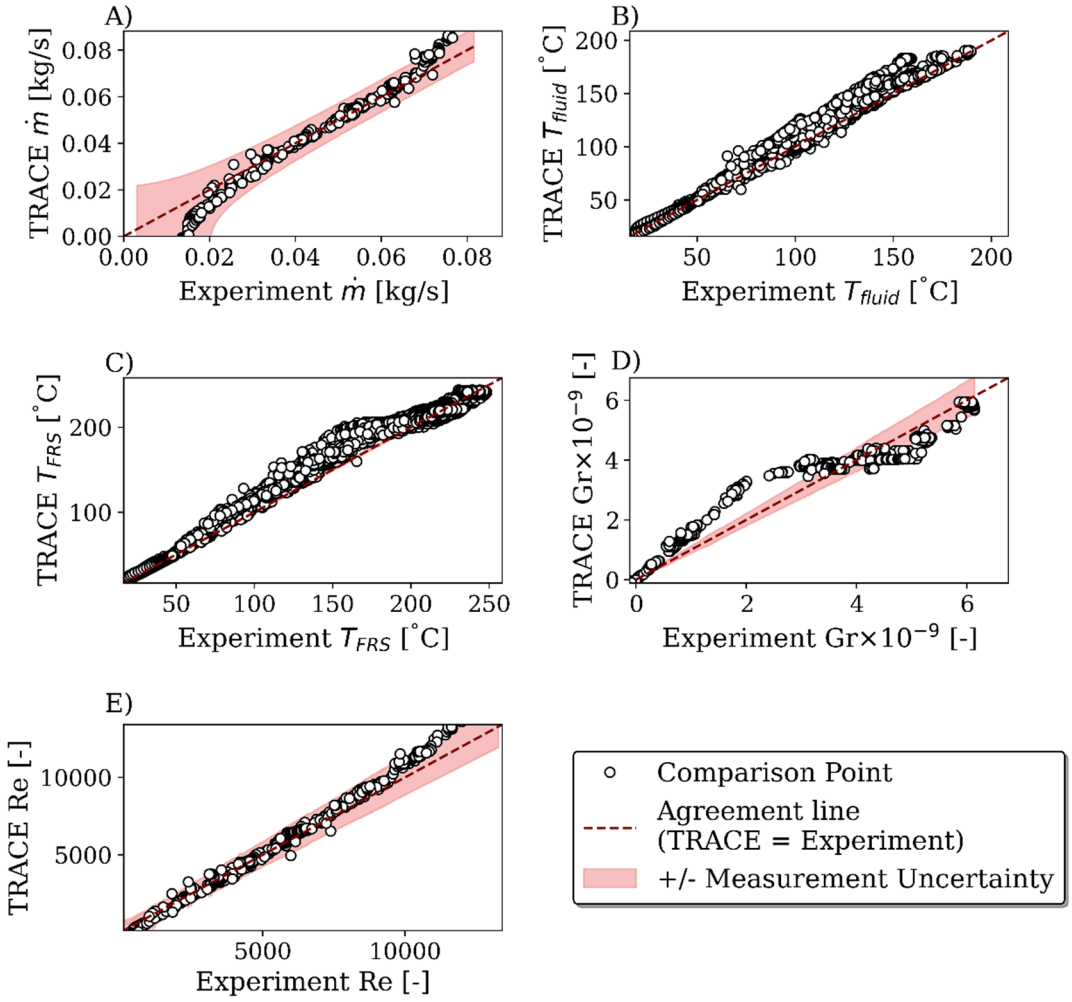

Figure 31. TRACE-to-experiment comparison for the entire experimental program. Comparisons are made for (A) mass flow rates, (B) fluid temperatures, (C) FRS temperatures, (D) Grashof numbers, and (E) Reynolds numbers.

Table 4. rRMSE for TRACE predictions relative to experimental data.

Parameter	rRMSE (%)
$\dot{m}$	7.79
T_{fluid}	2.46
T_{FRS}	2.95
Gr	20.6
Re	11.6

Figure 31 shows that the FRS temperatures predicted by TRACE are consistently greater than the experimental measurements up to approximately 200°C where the agreement improves. The same is true for the fluid temperature predictions, and the differences in these parameters could be causing the larger discrepancies in the Grashof number predictions because most of the terms in the Grashof number calculation depend on temperature or a temperature-dependent property. The rRMSE values shown in Table 4 are similar to those reported in Gorton et al. (2022) for TRACE comparisons to experimental data from the previous thermosyphon design. The mass flow rate predictions in this work are slightly more erroneous than those reported in Gorton et al. (2022). However, a parametric study on friction factor correlations was included in that work to find the correlation that minimized the mass flow rate rRMSE, whereas the TRACE default correlation was used in this work.

4. SUMMARY AND CONCLUSIONS

This report summarizes a series of experiments conducted in an updated thermosyphon cartridge loop with geometry relevant to VTR irradiation sites. Comparisons were made to experiments conducted by using a previous iteration of the cartridge design and with TRACE thermal hydraulics models. The experimental program was designed to resemble potential operating conditions in the VTR, and the purpose of the experiments was to characterize the cartridge hydraulic conditions during steady-state and transient tests. These experiments support the qualification of potential future experiments in the VTR, and the code-to-experiment comparisons support the qualification of TRACE for design and safety calculations.

Compared with the previous thermosyphon design, the updated cartridge had larger hydraulic diameters, which contributed to enhanced heat removal and greater minimum-to-maximum water temperature differences in the cartridge loop. Natural circulation mass flow rates were somewhat greater in the updated design, although the lower operating temperatures led to relatively similar Reynolds numbers between the two designs because water viscosity was the most sensitive parameter in the Reynolds number equation. Grashof numbers in the rodded region of the baffle pipe were significantly greater in the updated design because of the dominance of the D_h^3 term in the Grahsof number equation, although the values were again approximately equivalent in the empty baffle region. Direct comparisons between previous TSTL experiments and the current experiments could not be made for the power ramp and rapid loss of external flow test types. The experiments conducted in the updated cartridge were analyzed, and the cartridge was shown to withstand power ramps up to 20 kW and external loss of flow tests at 20 kW without exceeding the 225-psig pressure limit or boiling.

The code-to-experiment comparisons with TRACE showed that the modeling tool could accurately predict hydraulic conditions in the cartridge loop under a variety of scenarios. The rRMSE for the TRACE fluid and FRS temperatures was less than 3% when considering the entire experimental program. The rRMSE for the simulated natural circulation mass rate was approximately 8%. The agreement between the code and the experiments could be improved if a parametric analysis were used to select an optimal friction factor correlation. The Reynolds and Grashof number rRMSE values were 11.6% and 20.6%, respectively. These larger errors are primarily caused by the compounding effects of errors in the temperature predictions and the temperature-dependent water properties. Overall, TRACE predictions strongly correlated with experimental data, and the comparisons support the use of TRACE for future cartridge loop design and analysis. Additional future work could include the use of computational fluid dynamics to cross-validate the TRACE results and identify sources of error in the 1D analysis.

5. ACKNOWLEDGMENTS

This work was funded by the US Department of Energy's (DOE) Office of Nuclear Energy (NE) VTR project. The reported work resulted from studies that support a VTR conceptual design, cost, and schedule estimates for DOE NE to make a decision of procurement. As such, it is preliminary.

6. REFERENCES

Balderrama Prieto, S. A., Sabharwall, P. & Farmer, M., 2019. *Natural Circulation of Sodium, Lead, LBE, Helium and Molten Salt Cartridge Closed Loops.* Portland, OR, 18th International Topical Meeting on Nuclear Reactor Thermal Hydraulics (NURETH 2019).

Gorton, J. P., Sweeney, D. C., Petrie, C. M. & McDuffee, J. L., 2022. Simulation of natural circulation cartridge loop experiments and application to molten salt reactors. *Submitted to Nuclear Engineering and Design.*

Hunning, A. J., Greenwood, M. S., McDuffee, J. M. & Thoms, K., 2019. *Design and Modeling of a Liquid-Fuel Salt Experiment for the Versatile Test Reactor.* Washington, D.C., Transactions of the American Nuclear Society, Vol. 121.

Jones, K., Rothe, J. & Dunsford, W., 2009. *Symbolic Nuclear Analysis Package (SNAP): Common ApplicationFramework for Engineering Analysis (CAFEAN) Preprocessor Plug-in Application Programming Interface Main Report,* NUREG/CR-6974, Vol. 1: U.S. Nuclear Regulatory Commission.

McDuffee, J., Felde, D. & Carbajo, J., 2017. *Design and Testing for a New Thermosyphon Irradiation Vehicle,* ORNL/TM-2017/399: Oak Ridge National Laboratory.

McDuffee, J. et al., 2019. *Flow Test Plan to Support the Development of Cartridge Loops in the Versatile Test Reactor.* Washington, D.C., United States, Transactions of the American Nuclear Society.

Petrie, C. M. et al., 2020. Single-phase, natural circulation annular flow measurmeents for cartrdige loop irradiation experiments. *Nuclear Engineering and Design,* Volume 370, p. 110900.

U.S. NRC, 2017. *TRACE V5.0 Patch 5 Theory Manual: Field Equations, Solution Methods, and Physical Models,* Washington, D.C., USA: Office of Nuclear Regulatory Research, Division of Safety Analysis .

Wachs, D. et al., 2018. *Development of Experimental Capabilities for Fuels and Materials Testing in the Versatile Test Reactor.* Orlando, Florida, Transactions of the American Nuclear Society, Vol. 119.